

Preferred crystal plane electrodeposition of aluminum anode with high lattice-matching for long-life aluminum batteries

Received: 27 September 2023

Accepted: 15 July 2024

Published online: 01 August 2024

Shixin Wang¹, Yuan Guo¹, Xianfeng Du¹✉, Lilong Xiong¹, Zhongshuai Liang¹, Mingbo Ma¹, Yuehong Xie¹, Wenzhi You¹, Yi Meng¹, Yifan Liu¹ & Mingxia Liu¹

Aluminum batteries have become the most attractive next-generation energy storage battery due to their advantages of high safety, high abundance, and low cost. However, the dendrite problem associated with inhomogeneous electrodeposition during cycling leads to low Coulombic efficiency and rapid short-circuit failure of the aluminum metal anode, which severely hampers the cycling stability of aluminum battery. Here we show an aluminum anode material that achieves high lattice matching between the substrate and the deposit, allowing the aluminum deposits to maintain preferred crystal plane growth on the substrate surface. It not only reduces the nucleation barrier of aluminum and decreases electrode polarization, but also enables uniform deposition of aluminum, improving the cycling stability of aluminum batteries. Aluminum anode with (111) preferred crystal plane can stably 25000 cycles at the current density of 5 A·g⁻¹, with a capacity retention rate of over 80%.

In recent years, battery energy storage systems have gradually gained prominence in the field of energy storage due to their advantage, such as the advantages of high energy utilization efficiency, flexibility of use and high responsiveness^{1–3}. Currently, lithium-ion batteries occupy the largest market share in the field of electrochemical energy storage^{4,5}, but lithium-ion batteries are difficult to enjoy in the energy storage market exclusively due to low raw material reserves and potential safety hazards. Therefore, it is imperative to find a next-generation electrochemical energy storage battery with abundant raw material reserves, high safety, and high stability. Based on this point, metal-ion batteries such as sodium, magnesium, aluminum, potassium, calcium, and zinc have gradually become the research hotspots for researchers all over the world^{6–11}. Among them, aluminum battery stands out from them due to their advantages such as high theoretical capacity (2981 mAh·g⁻¹), high abundance, high safety, and low cost^{12,13}. However, the dendrite problem associated with inhomogeneous electrodeposition during repeated cycling leads to low Coulombic efficiency and rapid short-circuit failure of the aluminum metal anode, which severely hampers the cycling stability of the aluminum battery.

Recently, researchers have guided the uniform deposition of metal anodes by constructing artificial surface layers (SEI layers)¹⁴, modulating electrolyte compositions and additives^{15,16} and modulating electrode structures¹⁷, et al. These approaches, although they have had some success, have been achieved by altering the base structure of the original aluminum foil or introducing other substances, which not only increases the cost of the electrodes, but also results in poor scalability due to the cumbersome process. Therefore, it is important to design an aluminum anode material based on the aluminum itself alone that can stably cycle during continuous aluminum electroplating/stripping processes and has a simple preparation process.

The electrodeposition process of metals is divided into the adsorption of metal ions and the anodic electro-crystallization of metal atoms¹⁸. However, during the electro-crystallization of metal atoms, metal crystals are constantly formed on the electrode surface and the state is constantly changing, which predetermines the diversity and complexity of the metal electrodeposition process^{19,20}. The structure of the deposited layer is closely related to the nucleation and growth of grains during the electro-crystallization process, as well as to the crystalline state of the deposited substrate surface²¹. For example,

¹Engineering Research Center of Energy Storage Materials and Devices, Ministry of Education, School of Chemistry, Xi'an Jiaotong University, Xi'an 710049, P. R. China. ✉e-mail: xianfengdu@mail.xjtu.edu.cn

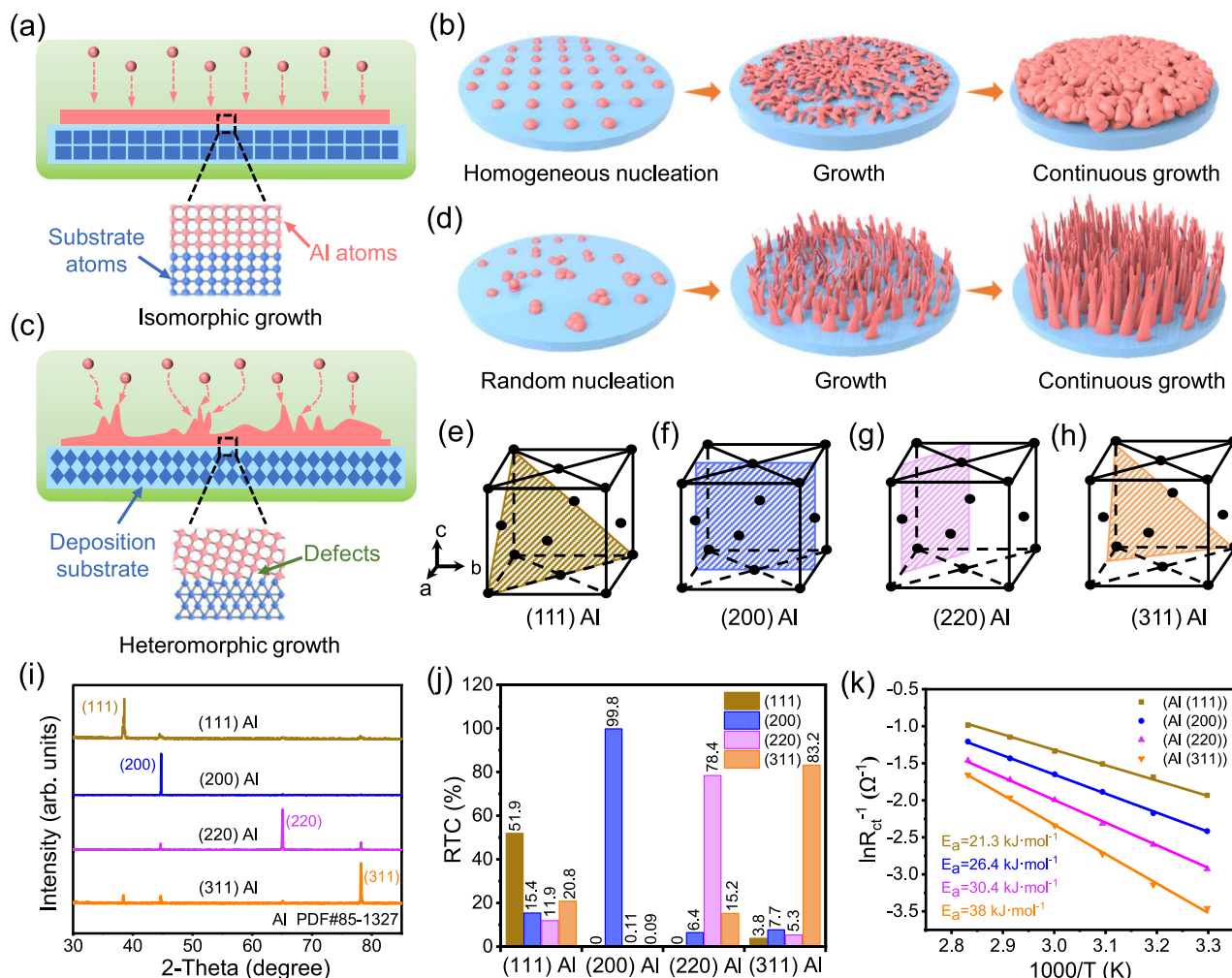


Fig. 1 | Design concepts for optimal crystal plane growth mechanism.

a Schematic diagram of isomorphic crystal plane growth. **b** Electrodeposition schematic representation of the homogeneous nucleated state. **c** Schematic diagram of heteromorphic plane growth. **d** Electrodeposition schematic representation of the random nucleated state. **e–h** Surface atomic arrangements. **i** XRD patterns and **j** histograms for the corresponding fitted RTC. **k** The activation energies of the different aluminum anodes.

representation of random nucleated state. **e–h** Surface atomic arrangements. **i** XRD patterns and **j** histograms for the corresponding fitted RTC. **k** The activation energies of the different aluminum anodes.

Cai et al. successfully achieved uniform and dense electrodeposition by selecting Ni substrate with a high lattice matching with Cu to support the Cu sediment²². In addition, previous studies have found that aluminum tends to form (111) crystal planes during electrodeposition due to its lower surface energy²³. Therefore, if aluminum with (111) preferred crystal planes is chosen as the anode, the lattice matching between the substrate and the deposited metal can be improved so that aluminum deposits can maintain uniform deposition on the surface of the aluminum substrate.

In this work, a stable and simple preparation process for aluminum battery anodes is reported by modulating the preferred orientation of the aluminum crystal plane, and demonstrate the correlation between the preferred crystal plane growth mechanism with high lattice matching and the electrochemical performance of aluminum anodes. The results show that this Al anode with (111) preferred crystal plane plays an important role in the initial nucleation and growth process of aluminum. Aluminum battery assembled with (111) Al anode have a more stable deposition morphology and longer cycle life, and have successfully achieved highly reversible deposition/plating, dendrite-free and high Coulombic efficiency simultaneously. Al anode with (111) preferred crystal plane is stably 25,000 cycles at the current density of 5 A·g⁻¹, with a capacity retention rate of over 80%. This work has opened a path for the development of rechargeable aluminum

batteries with high stability, and is of great significance for the development of high safety energy storage batteries.

Results and discussion

Since the reaction on the surface of the aluminum anode is mainly the plating and stripping of aluminum, its electrochemical properties are influenced by the atomic structure of the anode surface. Aluminum has a face-centered cubic structure, with significant changes in each crystal plane. The arrangement of atoms varies on different crystal planes, which has different effects on the rate of crystal growth²⁴.

Figure 1a shows the schematic diagram of isomorphic crystal plane growth on the same crystal plane. For isomorphic crystal plane growth, the electrodeposition process is more about the continued growth of the original crystal, and the deposition substrate will act as an aluminophilic site to better interact with aluminum atoms. Figure 1b is the schematic diagram of aluminum electrodeposition in isomorphic crystal plane growth mode. It can be seen from the Figure that due to the sediment and the substrate are the same crystal orientation, the deposition layer on the electrode surface exhibits good uniformity. On the contrary, if the deposited substrate and sediment have different preferred crystal plane orientations, they will produce defects due to partial exclusion. In this case, aluminum

will randomly nucleate on the surface of the substrate, and the deposition process will always be in an uncontrollable state, thereby inducing the growth of Al dendrites (Fig. 1c, d). Figure 1e–h is the surface atomic arrangements of the (111), (200), (220), and (311) crystal faces of Al. It can be seen from the figure that the number and arrangement of atoms on different crystal planes are different, which means that when aluminum with different preferred crystal plane orientations is used as the deposition substrate, there will be differences in the deposition morphology of aluminum.

In order to explore the influence of different preferred crystal plane aluminum substrates on aluminum deposition behavior, we prepared (111) Al, (200) Al, (220) Al, and (311) Al anodes by rolling and thermal annealing methods. The detailed preparation process is shown in Supplementary Fig. 1. Firstly, aluminum metal crystals will undergo irreversible plastic deformation under mechanical rolling, so that the metal atoms at the lattice nodes will produce relative slip. This relative slip will cause distortion of the original lattice, resulting in the original grains are broken into fine grains at the microscopic level. Annealing the aluminum foil at this time can eliminate internal stress and improve lattice defects, and fine grains can also regrow, ultimately causing the crystal transformation of the aluminum. Supplementary Fig. 2 indicates that moderate rolling may have a partial impact on the grain layout, but it will not affect the crystal orientation of the aluminum foil. XRD patterns (Fig. 1i) indicate that the prepared four preferred orientation aluminum foil exhibit the peaks at 38.4°, 44.7°, 65.1°, and 78.2° corresponding to (111), (200), (220), and (311) crystal planes, respectively²⁵. These peaks are consistent with the data from the standard comparison card (PDF # 85-1327). For ease of differentiation, we label the corresponding aluminum foil as (111) Al, (200) Al, (220) Al, and (311) Al. The relative texture coefficient (RTC) of each facet is calculated based on the following formula:

$$RTC_{(hkl)} = \frac{I_{(hkl)}/I_{0(hkl)}}{\sum I_{(hkl)}/I_{0(hkl)}} \times 100\% \quad (1)$$

where $I_{(hkl)}$ is the intensity obtained from the actual sample, and $I_{0(hkl)}$ is the intensity of the standard-oriented sample. Histograms and detailed calculation process for the corresponding fitted RTC are shown in Fig. 1j and Table S1. The results show that the relative texture coefficients of (111) Al, (200) Al, (220) Al, and (311) Al anodes are 51.9, 99.8, 78.4%, and 83.2%, respectively, which further quantifies the differences in preferred crystal planes orientation of the selected aluminum foil. Supplementary Fig. 3 shows the surface SEM images and EDS data of four preferred orientation aluminum foil. It can be seen from the corresponding SEM images that there are slight differences in the surface textures of the different aluminum foils, which may be caused by different stacking methods of aluminum grains on different crystal planes. The EDS data shows that the four kinds of preferred orientation Al anodes only contain Al and O elements, and the element content is basically similar, indicating that the purity of the four kinds of preferred orientation Al anodes is consistent, without other impurity elements. Next, we investigated the dynamic processes of four types of preferred orientation Al anodes in ionic liquid electrolytes. Supplementary Fig. 4 shows the electrochemical impedance spectroscopy test results of symmetrical batteries assembled with the different preferred orientation Al at different temperatures after the CV test (The fitted data were displayed in Table S2). It can be clearly seen from the Figure that the charge transfer resistance (R_{ct}) of (111) Al anode at different temperatures is significantly lower than that of the other three Al anode. In addition, the dynamic process of electrodeposition on the electrode surface is related to the reaction activation energy on the anode surface^{26,27}. The activation energy calculated by the Arrhenius equation generally refers to the energy absorbed by non-activated molecules to transform into

activated molecules. The activation energy of each preferred orientation Al can be calculated by the Arrhenius equation:

$$\frac{1}{R_{ct}} = Ae^{-\frac{E_a}{RT}} \quad (2)$$

Where, R_{ct} is the charge transfer resistance, A is the frequency factor, R is the gas constant, and T is the absolute temperature. As is shown in Fig. 1k, the calculated activation energies of (200) Al, (220) Al, and (311) Al are 26.4, 30.4, and 38 kJ·mol⁻¹, respectively, while (111) Al anode shows a lower activation energy (21.3 kJ·mol⁻¹), which indicates that (111) Al anode has more excellent charge transfer kinetics characteristics²⁸.

In order to investigate the relationship between the morphology and crystal structure of aluminum deposits more systematically, we assembled symmetrical batteries using (111) Al, (200) Al, (220) Al, and (311) Al anodes. Figure 2a are the optical photos (Fig. 2a inset) and XRD results of the separator surface after first-cycle Al plating at the areal special capacity of 15 mAh·cm⁻² and the areal current density of 1 mA·cm⁻². Figure 2a inset shows that a large amount of aluminum deposits adheres to the surface of the glass fiber separator at the large surface capacity of 15 mAh·cm⁻². This is mainly due to the loose deposition morphology prevents deposit form a foil shape. Therefore, the crystal face and morphology of aluminum deposits can only be observed from the separator side. It can be seen from the XRD test results that the sediment of four preferred orientations Al exhibit characteristic peaks corresponding to the (111), (200), (220) and (311) crystal planes of aluminum at 38.4°, 44.7°, 65.1°, and 78.2°, respectively. The XRD results of the four preferred orientations Al are completely consistent with the standard PDF card values of aluminum (PDF#85-1327), indicating that the Al deposits on the separator surface have high purity. In addition, the XRD spectra of the Al deposit on the surface of the four separators show a strong orientation of the (111) crystal plane, indicating that aluminum deposited on the electrode surface tends to grow along the (111) crystal plane.

Figure 2b–e shows the SEM image of the separator surface in a fully charged state. It can be clearly seen from the figure that when (111) Al is used as the electrode, the morphology of the glass fiber can still be seen on the surface of the separator (Supplementary Fig. 5 is SEM images of the original separator). In addition, as is shown in Supplementary Fig. 6, the Si, O, and Na elements content of the separator surface on the (111) Al electrode side are significantly higher than those of other preferred orientation Al, indicating that most of the aluminum is deposited on the electrode surface rather than on the separator surface. This result also indicates that aluminum deposits have better bonding strength on the surface of the (111) Al electrode. On the contrary, when (200) Al, (220) Al, and (311) Al is used as electrodes, thick and uneven Al deposits appear on the surface of the separator, and the morphology of the glass fiber is also close to disappearing. This is mainly due to the loose morphology of the Al deposits caused by heterogeneous growth, thereby cannot bind well with the substrate. During the disassembly process of the battery, most of the Al deposits adhere to the surface of the separator, covering the original morphology of the glass fiber separator. The purity and elemental distribution of Al deposits can be obtained from SEM mapping (Fig. 2f–i). It can be seen from the figure that the distribution of aluminum elements is more uniform when (111) Al is used as the electrode compared with the other three preferred orientation Al anodes. This is mainly because in the isomorphic crystal plane growth mode, the electrodeposition process is mainly vertical growth in situ on the original substrate, and the deposition substrate can better interact with Al atoms as an aluminophilic site, so as to achieve uniform deposition of Al. In addition, the (200) Al anode also exhibits a uniform distribution of aluminum elements, but the thicker Al deposit on the separator surface will increase the risk of battery short-circuit failure. A small

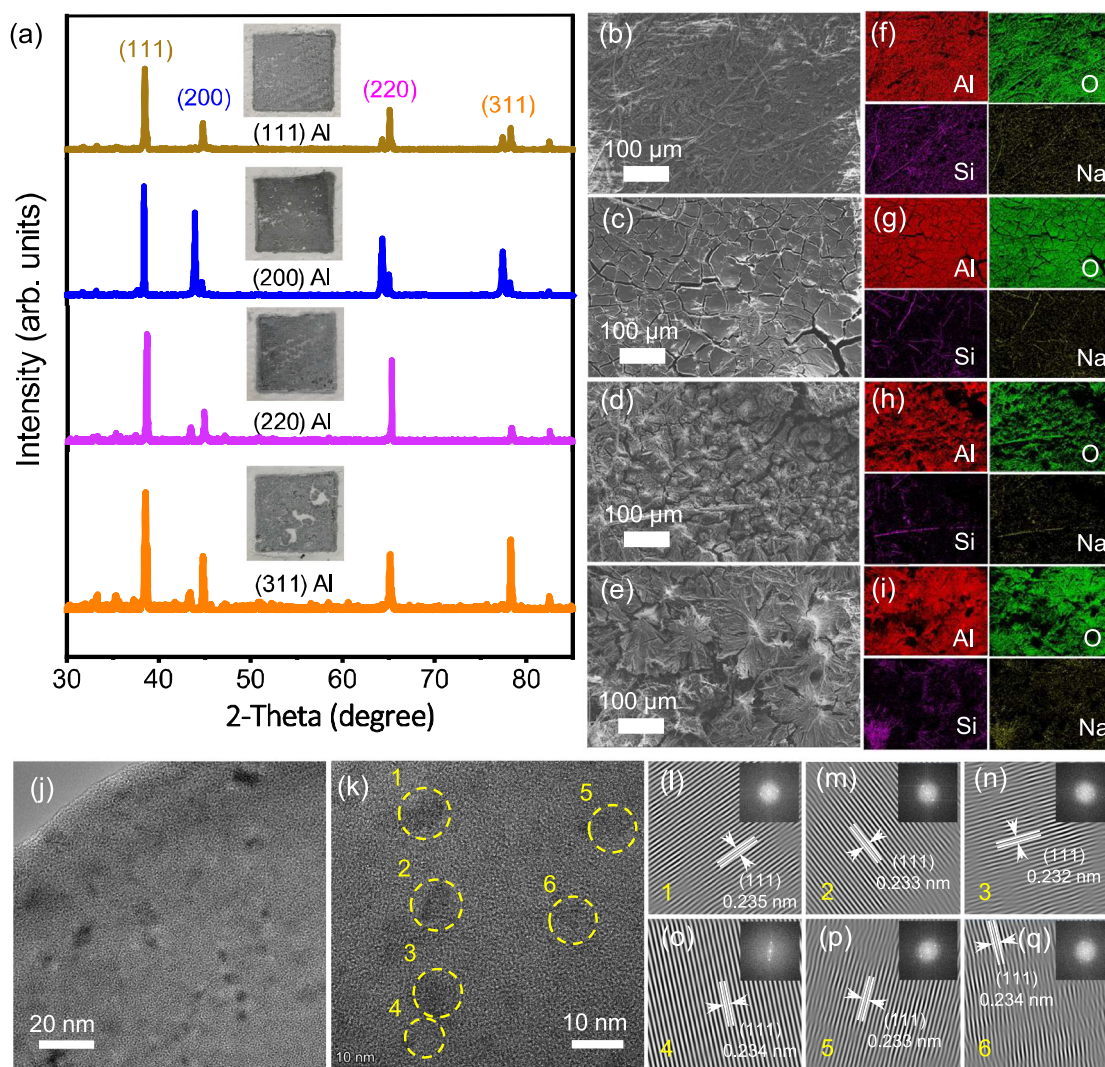


Fig. 2 | Morphological and structural characterization of aluminum metal deposits. **a** The XRD spectra and optical photograph of the separator side. **b–e** SEM images and **f–i** elements mapping of the separator surface. **j** TEM images of the (111)

Al anode surface. **k** HRTEM images of the (111) Al anode surface. The fitting process corresponds to the 1 (**l**), 2 (**m**), 3 (**n**), 4 (**o**), 5 (**p**), and 6 (**q**) of Fig. 2b.

amount of O, Si, and Na elements also appeared in the EDS analysis. The sample of the EDS-Mapping test was tested on the surface of glass fiber, which is made of sodium borosilicate (Na_2SiO_3). Therefore, the oxygen element appears in the EDS-Mapping test results. Si and Na are also the main elements of the separator. Therefore, in order to obtain a more uniform aluminum deposit, it is naturally the best choice to directly perform preferred crystal plane growth on the surface of (111) preferred orientation Al.

The nucleation process of aluminum can be divided into three steps:

- (1) In the early stage of Al deposition, the Al_2O_3 film tends to be consumed by ionic liquids, while forming a stable electrode/electrolyte interface.
- (2) Nucleation occurs under a stable SEI layer, further leading to the deposition of aluminum.
- (3) As the deposition time prolongs, the grains gradually grow.

To demonstrate this process, we tested the XPS spectroscopy of the electrode surface in the initial state and after cycles. As is shown in Supplementary Fig. 7, it can be clearly seen from the graph that the XPS test results show only Al-O bonds of alumina in the initial state. However, the XPS spectroscopy of the symmetric battery after cycles not

only shows Al-O bonds, but also appears Al-Al bonds representing Al metal. This is mainly due to the large amount of aluminum being leaked after the natural alumina on the electrode surface is consumed by the ionic liquid. From the XPS spectrum of the Cl element, there are peaks corresponding to Cl-Al and Cl-O bonds on the electrode surface after cycling, which proves the formation of the SEI layer. The XPS results in Supplementary Fig. 7 indicate that the formation process of the SEI layer on the surface of all preferred crystal planes aluminum foil is basically consistent, formed by Al-Cl and Al-O bonds. Supplementary Figs. 8, 4 is the electrochemical impedance spectroscopy at different temperatures in the initial state and after CV test of the symmetric battery (The fitted data is displayed in the Table S3). In an initial state, the impedance values of symmetric batteries assembled with different preferred crystal face electrodes are very large, reaching several thousand ohms at room temperature (Supplementary Fig. 8a–d). After the CV test, the impedance values of symmetric batteries assembled with different preferred crystal face electrodes significantly decrease (Supplementary Fig. 4a–d), which is mainly due to the formation of a stable electrode/electrolyte interface on the electrode surface after the consumption of alumina. The symmetric batteries assembled with the (111) Al have the minimum charge transfer resistance, indicating faster charge transfer kinetics process.

After the formation of the SEI layer, aluminum nucleation and growth processes occur. During this process, the atomic arrangement of the aluminum substrate will have an impact on the later deposition process. The structure, morphology, and composition of the (111) Al anode surface before and after the Al stripping/plating process was verified by high-resolution field emission transmission electron microscope images. Supplementary Fig. 9a shows the HRTEM image of the (111) Al anode surface in its initial state, from which a clear lattice structure is observed. The FFT diagram from Supplementary Fig. 9b shows three types of lattices spacing, with lattice of 0.232 nm corresponding to the (111) crystal plane of aluminum (Supplementary Fig. 9c–e), lattice of 0.202 nm corresponding to the (200) crystal plane of aluminum (Supplementary Fig. 9f–h), and another blurred lattice possibly corresponding to the (220) or (311) crystal plane of aluminum (Supplementary Fig. 9i–k). Among them, the lattice pattern of the (111) crystal plane corresponding to aluminum is clearer, indicating that the preferred crystal plane of the (111) Al anode is the (111) crystal plane. This is consistent with the XRD results of (111) Al anode. Figure 2j, k shows the TEM and HRTEM images of the (111) Al anode surface in a fully charged state, from which many black particles can be observed. Six small particles were fitted based on the HRTEM results, as shown in Fig. 2l–q, the lattice spacing of almost all particles corresponds to the (111) crystal plane of aluminum, indicating that the aluminum particles grown on the (111) Al anode surface are all the (111) crystal planes of aluminum, confirming the preferred crystal plane growth of aluminum on the (111) preferred crystal plane. This process clearly demonstrates the preferred crystal plane growth of aluminum on the (111) Al anode surface.

In order to further understand the matching mechanism between Al deposits and substrate lattices during preferred crystal plane growth process, we calculated the binding energy for aluminum atom and Al substrates with different main crystal planes using density functional theory (DFT). Supplementary Fig. 10 shows the structural diagram of aluminum atoms arranged in different crystal planes. As is shown in the Supplementary Figs. 11, the binding energy for the deposition of aluminum atoms with the base on the surface of (111) Al, (200) Al, (220) Al, and (311) Al anodes is -6.65 , -7.15 , -7.24 , and -7.79 eV, respectively. Obviously, the Al atoms deposited on the surface of the (111) Al electrode bind more firmly to the substrate, which means the aluminum deposits on the surface of the (111) Al electrode are less likely to detach from the substrate. Due to the adhesion of aluminum deposits to the surface of the partition, it can accelerate the occurrence of battery short-circuit faults. Therefore, a stronger binding energy between aluminum and the substrate will be more conducive to subsequent electroplating/stripping reactions. Figure 4a–d can also prove this point. After 50 cycles, only the Al deposits on the surface of the (111) crystal plane aluminum electrode did not adhere to the separator among the four preferred crystal planes of the anode, which also matches the calculation results.

In order to systematically study the effect of different preferred orientations Al on the stability of Al plating/stripping process, we conducted galvanostatic charge-discharge test of symmetric cells assembled with (111) Al, (200) Al, (220) Al, and (311) Al anodes. Figure 3a–d shows the polarization voltage curves of Al/Al symmetrical cells assembled with (111) Al, (200) Al, (220) Al, and (311) Al electrodes under the areal special capacity of $1 \text{ mAh}\cdot\text{cm}^{-2}$ and the areal current density of 1 , 2 , 5 , and $10 \text{ mA}\cdot\text{cm}^{-2}$. It can be seen from the figure that when the current density transfers from 0.5 to $1 \text{ mA}\cdot\text{cm}^{-2}$, symmetrical cells assembled with (220) Al and (311) Al electrodes exhibit short-circuit signals one after another²⁹, and (200) Al anodes can only operate stably for 12 h at the current density of $2 \text{ mA}\cdot\text{cm}^{-2}$. On the contrary, symmetrical cells with (111) Al anode can maintain stable polarization voltage at different current densities. Even when the current density is converted to $10 \text{ mA}\cdot\text{cm}^{-2}$, (111) Al anode still exhibits stable Al plating/stripping behavior, indicating that (111) Al anode can promote the plating and

stripping of Al and extend the cycling life of the battery. In addition, symmetrical cells assembled with (111) Al anode can stably cycle for over 1900 h at the current density of $1 \text{ mA}\cdot\text{cm}^{-2}$ and the areal special capacity of $5 \text{ mAh}\cdot\text{cm}^{-2}$, which is 2.37, 2.43, and 17.2 times that of Al (200), Al (220), and Al (311) anode. This result is due to different Al deposition morphologies on the Al anodes of different preferred orientations.

Supplementary Fig. 12 shows the SEM images of the electrode surface with different preferred crystal faces at the areal capacity of 1 and $5 \text{ mAh}\cdot\text{cm}^{-2}$ after the first-cycle Al plating. It can be seen from the images that the deposition morphology of aluminum on different Al anode surfaces. When the areal capacity is $1 \text{ mAh}\cdot\text{cm}^{-2}$, the deposition morphology of the (111) Al electrode surface is uniform micrometer scale cluster particles, the aluminum particles on the (200) Al electrode surface are microsphere like and randomly dispersed, (220) Al and (311) Al electrodes surface exhibit randomly distributed dendritic dendrites. As the areal capacity increases to $5 \text{ mAh}\cdot\text{cm}^{-2}$, the particle distribution on the surface of (111) Al anode remains uniform and dense, and the average particle size remains almost unchanged. On the contrary, different morphology of dendrites appeared on the surfaces of the other preferred orientations Al, indicating that the (111) crystal faces of aluminum are favorable for the electrochemical performance of the aluminum batteries. In addition, (111) Al anode surface on the side of aluminum stripping exhibits a uniform linear stripping morphology, while other preferred orientation Al surfaces show randomly stripping morphology, and electrode corrosion is more severe. This is mainly due to the morphological differences in isomorphous crystal plane growth and heteromorphous growth of aluminum.

In addition, the early nucleation state of metals plays an important role in studying the deposition mechanism of metal battery anodes³⁰. According to the theory of metal nucleation, the nucleation of solid phases requires overcoming a free energy barrier³¹. The nucleation barrier of metal is also closely related to the nucleation overpotential. When the metal begins to plate, an obvious voltage drop will be observed, followed by a flat voltage platform. The nucleation overpotential is the voltage difference between the lowest point voltage and the highest flat section in the voltage polarization curve. The smaller the polarization voltage, the lower the metal nucleation barrier³². Once the nucleation overpotential is overcome, the energy required for the aluminum deposition process decreases until the deposition state stabilizes. In order to evaluate the role of (111) Al anode in the nucleation and growth process of metallic Al, we assembled a symmetric battery with four preferred oriented Al anodes and tested the nucleation behavior of Al on an electrode surface. Figure 3i shows time–voltage curve of Al/Al symmetrical cells assembled with (111) Al (e), (200) Al (f), (220) Al (g), and (311) Al (h) electrodes. It can be seen from the figure that the current density increases rapidly in the initial stage, which is mainly due to the formation of crystal nuclei near the electrode in the initial stage. As the thickness of the sediment continues to increase, the deposition process on the electrode surface gradually stabilizes, and the current gradually maintains a stable value. This is mainly due to the platform overpotential of aluminum electrodeposition. The nucleation time on the surface of (111) Al anode is the least compared to other preferred orientation anode. On aluminum foils with different main crystal planes, the (311) Al anode exhibits the highest nucleation overpotential at the same current density, while the (111) Al anode exhibits the lowest nucleation overpotential (93 mV). This indicates that the nucleation potential barrier on the surface of (111) Al electrode is the lowest, indicating that uniform and smooth aluminum deposition is more likely to occur on the electrode surface. Additionally, it can also be seen from Fig. 3g, k that the polarization voltage of (111) Al electrode is the smallest under both high current density and large area capacity, which is related to the unique isomorphous crystal plane growth mode of (111) Al electrode. The in situ growth of aluminum on the substrate can continuously regulate the electric field distribution of the

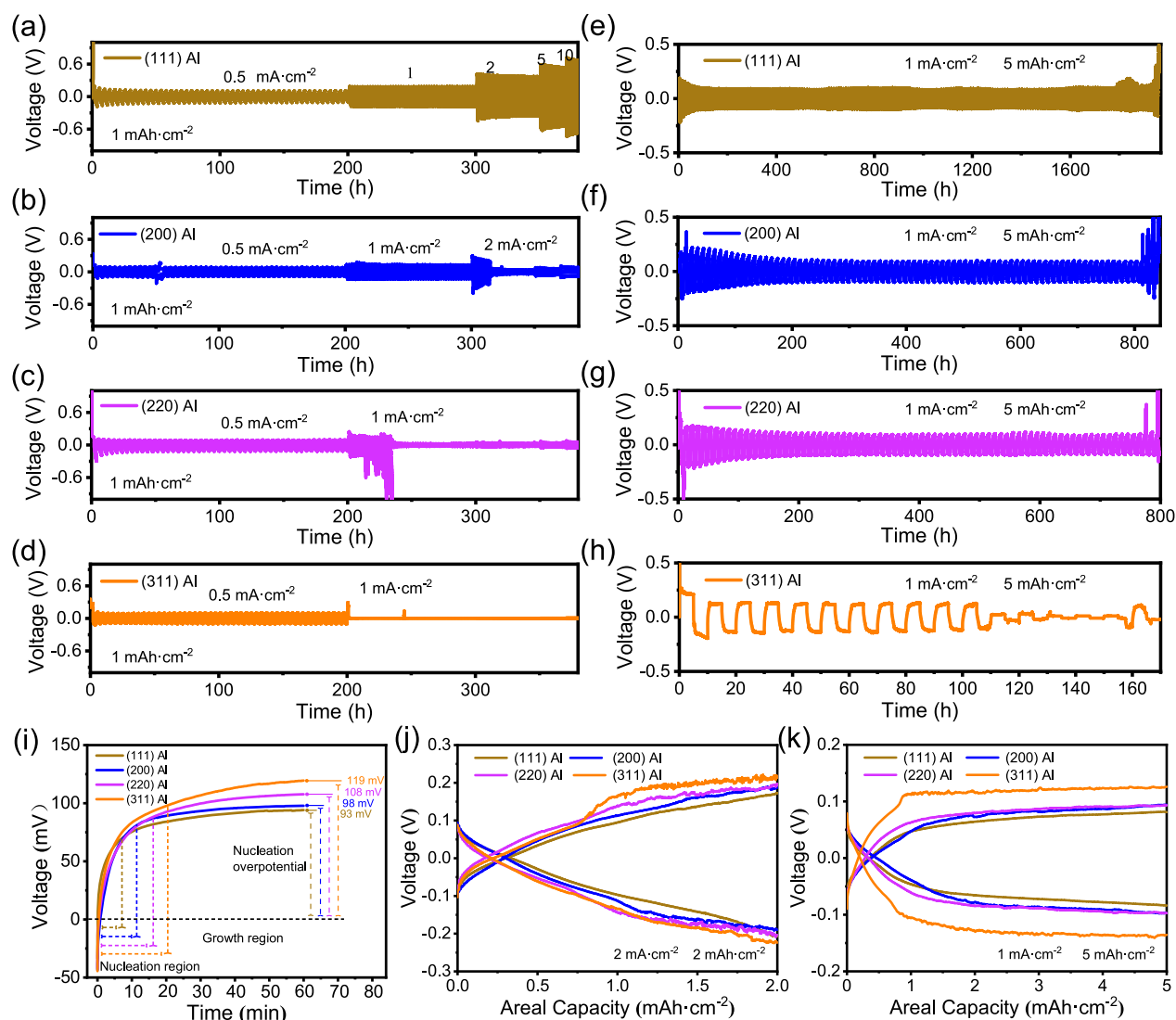


Fig. 3 | Electrochemical performance of symmetrical batteries. a–d Polarization voltage curves and **e–h** cycle performance of symmetrical cells. **i** Time–voltage curve. **j, k** The first-cycle Al deposition and dissolution curves of the symmetric cell at different test conditions.

electrode surface to be more uniform, inducing free-dendritic deposition of aluminum on the electrode surface, thereby extending the cycling life of the battery.

As is well known, the deposition morphology of metal on the electrode surface plays a decisive role in the battery life³³. Therefore, we studied the deposition morphology of four preferred orientations Al on the electrode surfaces through SEM after 50 cycles, and the corresponding SEM images are shown in Fig. 4a–d. It can be seen from Fig. 4a that the deposition morphology of aluminum on the surface of the (111) Al anode presents uniform sheet-like clusters, and no obvious aluminum deposition particles are visible on the corresponding side of the separator surface (Fig. 4e). This is mainly due to the high lattice matching between the Al deposit and the substrate caused by the isomorphic crystal plane growth mechanism, which induces the deposition particles to uniformly bond with the substrate and in situ growth in the substrate. Contrary to (111) Al anode, the surfaces of (200) Al, (220) Al and (311) Al anodes exhibit dimples of varying sizes, while the deposits all adhere to the separator surface near the electrode side (Fig. 4f–h). This is because the heteromorphic deposition mode tends to loosen the morphology of aluminum deposits, resulting in the inability to form foil-like structures. During the repeated cycling process, Al deposits on the separator surface

will aggregate to form dendrites and continuously grow towards the counter electrode, causing short-circuit failure of the battery. These results indicate that the high lattice matching between the sediment and (111) Al anode can regulate the nucleation and growth mechanism of Al, thereby enabling uniformly deposited on the electrode surface without dendrite growth.

As is shown in Supplementary Fig. 13, to demonstrate the uniform nucleation of aluminum on the (111) Al electrode surface, we tested the deposition morphology of aluminum electrode with different preferred crystal faces at lower areal capacities (0.1 mAh·cm⁻²) and current densities (0.1 mA·cm⁻²). The (111) Al electrode surface exhibits uniform deposition and small aluminum deposition particles. In sharp contrast, the other three electrode surfaces exhibit uneven deposition of Al particles, and the (311) Al electrode surface even exhibits obvious dendritic morphology. This indicates a uniform nucleation process on the surface of the (111) Al electrode. Supplementary Fig. 14 are the SEM image and XRD test result of (111) Al anode surface at full charge state after 100 cycles under the areal special capacity of 1 mAh·cm⁻² and the areal current density of 1 mA·cm⁻². The surface of the (111) Al electrode exhibits uniform deposition morphology after 100 cycles. In addition, as shown in Supplementary Fig. 14b, the preferred crystal plane on the surface of the (111) Al electrode remains the (111) crystal plane, and the

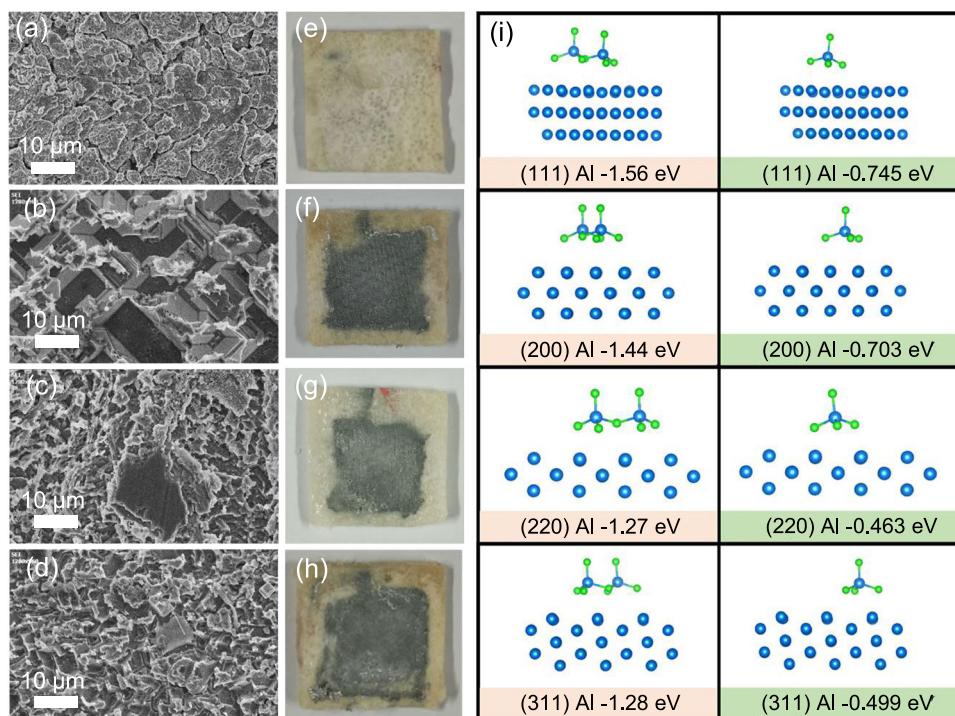


Fig. 4 | Analysis of the bonding strength between aluminum deposits and aluminum anode. a–d SEM images of different aluminum anode surfaces after 50 cycles. **e–h** The optical images of the separator surface corresponding to different

anodes after 50 cycles. **i** Calculation model and adsorption energy of AlCl_4^- and Al_2Cl_7^- on different aluminum anode surfaces.

preferred orientation remains largely unchanged. This indicates that there is no loss of advantageous crystal orientation during the continuous Al stripping/plating process.

In the electrodeposition process of aluminum, AlCl_4^- and Al_2Cl_7^- are the main ions involved in the reaction, so the strong adsorption ability of the deposition substrate for these two ions helps the electrodeposition reaction. Generally, adsorption energy (E_{ad}) refers to the energy released by the adsorption process between the adsorbate and the substrate³⁴. When the adsorption energy is negative, it indicates that the adsorption process can proceed spontaneously. The higher the absolute value of adsorption energy, the stronger the interaction between the adsorbate and the substrate³⁵. Figure 4i is the adsorption energy of AlCl_4^- and Al_2Cl_7^- ions on the surfaces of (111) Al, (200) Al, (220) Al, and (311) Al electrodes by DFT calculation. DFT results show that AlCl_4^- and Al_2Cl_7^- ions have higher adsorption energies on the surface of (111) Al anode, indicating stronger interaction between the (111) surface of Al and the substrate during the early deposition process. This means (111) Al anode can provide a stronger nucleation driving force for the subsequent deposition of Al.

In order to observe the dynamic growth process of Al on the surface of Al anodes with different preferred orientations more intuitively, we assembled an Al|Al symmetric cell and conducted in situ optical observation. The in situ observation device is shown in Fig. 5a. Two aluminum foils are used as electrodes, with an electrolyte added in the middle. Finally, the deposition behavior of aluminum is observed using the light microscope. The in situ observation images of four preferred orientation Al anode are shown in Fig. 5c–f, the corresponding in situ movie can be found in Supplementary Movies 1–4. The results showed that after the deposition time exceeded 15 min, non-planar and island-shaped deposition morphologies appeared on the surfaces of (200) Al, (220) Al, and (311) Al electrodes. In stark contrast, the (111) Al electrode surface exhibits uniform aluminum deposition morphology. In addition, after the deposition time reaches 60 min, it can be more clearly seen that the uniform and dense

deposition morphology of the (111) Al electrode, as well as the uneven deposition morphology of (200) Al, (220) Al, and (311) Al electrodes, which is consistent with test results shown in Supplementary Fig. 15. In addition, Fig. 5b shows the schematic diagram of isomorphous crystal plane growth mode. The Al deposit exhibits high lattice matching with the (111) Al anode, so Al atoms can easily interact with the substrate and grow uniformly along the substrate.

In order to illustrate the practical application of (111) Al anode in aluminum batteries, we assembled an Al|3DGr full battery using 3DGr as the positive electrode (1 mg cm^{-2}) and four preferred crystal plane Al as the negative electrode. Figure 6a, b show the porous structure and high crystallinity of 3DGr. As is shown in Fig. 6c, the full battery assembly with four preferred orientation Al anode all showed obvious oxidation peaks at 1.86, 2, and 2.29 V and corresponding reduction peaks at 1.58, 1.76, and 2.05 V, indicating their highly reversible electrochemical behavior³⁶. Figure 6d shows the electrochemical impedance spectroscopy (EIS) results of the full battery assembled with (111) Al, (200) Al, (220) Al, and (311) Al electrodes as negative electrodes, respectively. The fitting results are shown in Table S4. According to the fitting results, the charge transfer resistances (R_{ct}) of (111) Al electrodes are 31.81Ω , significantly lower than that of (200) Al, (220) Al, and (311) Al electrodes. This indicates that a full battery assembled with (111) Al electrodes exhibits faster Al stripping/electroplating reaction kinetics³⁷.

The results of the galvanostatic charge-discharge (GCD) curve are shown in Fig. 6e, f. The (111) Al|3DGr battery has higher capacity, wider voltage platform, and lower polarization voltage at both the current density of 1 A g^{-1} and 10 A g^{-1} . As is shown in Fig. 6g, the capacity of the four preferred oriented Al is basically the same when the current density is 1 A g^{-1} . However, when the current density increases to 10 A g^{-1} , the capacity of (111) Al, (200) Al, (220) Al, and (311) Al electrodes are 76.6, 60.4, 41.1, and 22.7 mAh g^{-1} , respectively. This further confirms that (111) Al electrodes are beneficial for improving the chemical reaction kinetics of Al plating/stripping. In addition, the (111) Al

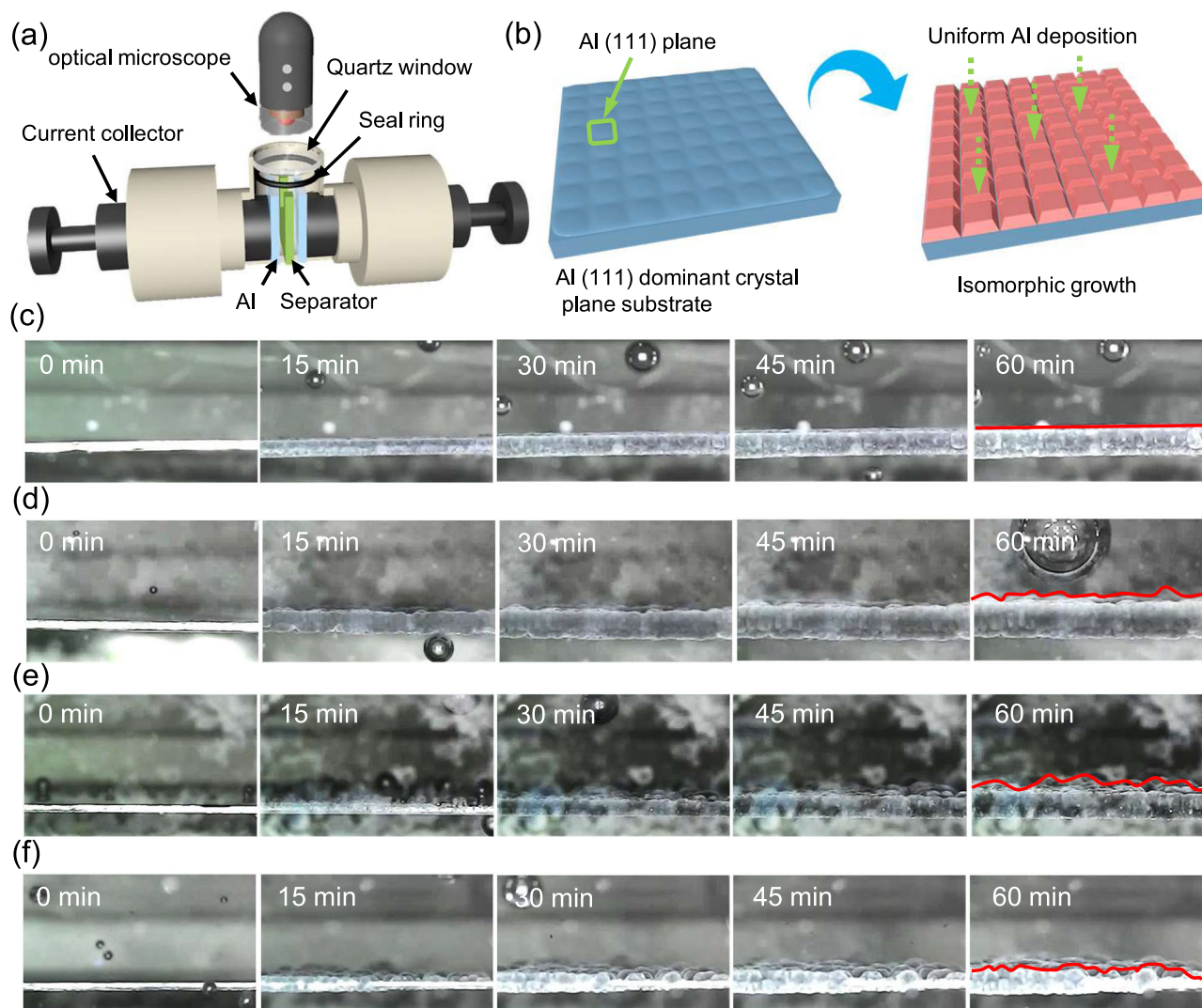


Fig. 5 | In situ optical observation images of aluminum anodes in plating process. a Diagram of in situ observation device. **b** Schematic diagram of isomorphic crystal plane growth mode. **c–f** In situ section optical observation of the plating process in different aluminum anodes.

electrode exhibited long-term cycling stability of 25,000 cycles at the current density of $5 \text{ A}\cdot\text{g}^{-1}$, and the capacity retention rate exceeded 80% (Fig. 6h). In contrast, the battery assembled with the other preferred orientation Al electrodes have short circuits failure after stable cycling for a period. The long cycle performance of (111) Al|3DGr battery is attributed to the highly reversible and aluminum deposition process of non-dendrites, while the formation of dead aluminum and dendrites in other preferred orientation Al anode during repeated cycles leads to poor electrode reversibility. These results confirm that the preferred crystal plane growth mechanism with high lattice matching can improve the possibility of achieving stable and dendrite-free high-performance aluminum batteries. In order to evaluate the application prospects of (111) Al anode, we assembled the pouch battery using flake graphite as the cathode ($15.7 \text{ mg}\cdot\text{cm}^{-2}$). Figure 6i is the capacity–voltage curve of the Al|FG pouch battery. It can be seen from the figure that even if the areal loading of the positive electrode active material is increased, the (111) Al|FG batteries still have a good voltage platform. As shown in Fig. 6j, the (111) Al|FG battery can still maintain the specific capacity of $80 \text{ mAh}\cdot\text{g}^{-1}$ at the current density of $20 \text{ mA}\cdot\text{g}^{-1}$. In addition, the pouch battery with (111) Al as the anode can provide a stable current to drive small fans and charge mobile phones (Fig. 6k, l), indicating that (111) Al anode-based aluminum batteries have enormous application potential. To further demonstrate the cycling

stability of the (111) Al anode at high areal capacity, we assembled the (111) Al|FG Swagelok battery with an areal loading of $15.5 \text{ mg}\cdot\text{cm}^{-2}$. As is shown in Supplementary Fig. 16a, the battery capacity is $87 \text{ mAh}\cdot\text{g}^{-1}$ at the current density of $20 \text{ mA}\cdot\text{g}^{-1}$. When the current density reaches $500 \text{ mA}\cdot\text{g}^{-1}$, the battery capacity can still reach $35 \text{ mAh}\cdot\text{g}^{-1}$. As shown in Supplementary Fig. 16b, the (111) Al|FG battery can maintain the specific capacity of $80 \text{ mAh}\cdot\text{g}^{-1}$, and stably cycle over 1000 cycles at the current density of $100 \text{ mA}\cdot\text{g}^{-1}$.

In summary, we verified the correlation between the preferred crystal plane growth mechanism of high lattice matching and the electrochemical performance of aluminum anodes by regulating the dominant crystal planes of aluminum substrates. It was determined that the (111) Al anode is advantageous for the electrochemical performance of aluminum battery by assembling symmetrical cells and a full battery. The role of the preferred crystal plane growth mechanism in the nucleation and growth process has been revealed through various experiments and DFT calculations. The deposition morphology of flat-plate on the surface of (111) Al anode greatly reduces the nucleation barrier of aluminum and improves the cycling stability of the aluminum anode. (111) Al anode can operate stably for over 1900 h even at the high areal capacity of $5 \text{ mAh}\cdot\text{cm}^{-2}$, which is 2.3–16.3 times that of other preferred orientation Al. In addition, the (111) Al anode can stably 25,000 cycles at the current density of $5 \text{ A}\cdot\text{g}^{-1}$, with a capacity retention

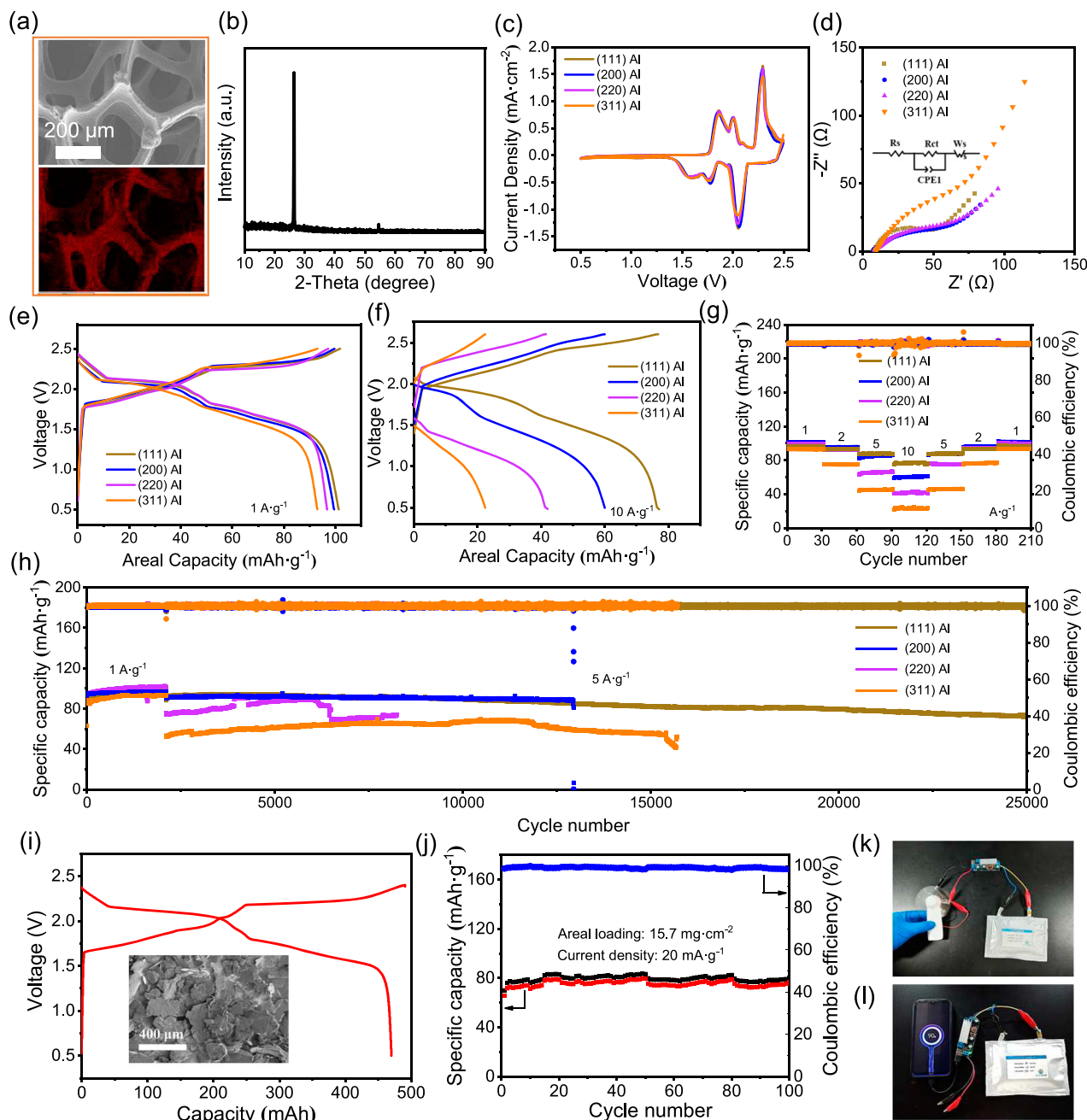


Fig. 6 | Electrochemical performance of aluminum anodes with different preferred crystal faces. **a** SEM images, element mapping and **b** XRD result of three-dimensional graphite. **c** CV curve and **d** Nyquist plot of Al|3DGr battery. **e, f** The GCD curves of Al|3DGr battery at different rates. **g** Rate performance of Al|3DGr

battery. **h** Long-term cycling tests of Al|3DGr battery. **i** Capacity-voltage curve and **j** cycle performance of (111) Al|FG pouch battery. **k, l** Application display of laminated pouch battery.

rate of over 80%. The preferred crystal plane growth mechanism of high lattice matching provides a direction for the development of high-stability and high-safety aluminum batteries.

Methods

Preparation of different preferred crystal plane anode

The (200) Al and (220) Al electrodes come from East Sunshine Aluminum Industry Co., Ltd. (99.99% purity, thickness is 120 μm). Preparation of (111) Al anode: Firstly, clean the aluminum foil with deionized water and acetone to remove any oil stains on the surface. Then, the roller press is used to roll the (220) Al to the deformation of 35% at the speed of 15 r/min (The temperature is 25 $^{\circ}\text{C}$). Next, the

rolled (220) Al was annealed at 350 $^{\circ}\text{C}$ in the vacuum environment for 30 min to obtain (111) Al anode. Among them, the vacuum degree should reach 3×10^{-3} Pa. Preparation of (311) Al anode: the roller press is used to roll the (200) Al to the deformation of 35% at the speed of 15 r/min (The temperature is 25 $^{\circ}\text{C}$). Next, the rolled (220) Al was annealed at 620 $^{\circ}\text{C}$ in the vacuum environment for 50 min to obtain (311) Al anode.

Preparation of ionic liquid electrolyte

The ionic liquid electrolyte in this paper is composed of anhydrous aluminum chloride (AlCl_3) and triethylamine hydrochloride (Et_3NHCl) with a molar ratio of 1.5:1³⁸. The anhydrous aluminum chloride is

analytically pure with a purity of 99.2% and was purchased from Sinopharm Group Co., Ltd., China. The triethylamine hydrochloride is also analytically pure with a purity of 99.5% and was purchased from Sinopharm Group Co., Ltd., China. Firstly, the triethylamine hydrochloride is placed in a vacuum drying oven at 130 °C to remove moisture. Secondly, 7.265 g of anhydrous aluminum chloride and 5 g of triethylamine hydrochloride are slowly added to a beaker and melted under magnetic stirring to form the ionic liquid. Then, the ionic liquid electrolyte is heated on the hot plate for 1 h to ensure the complete reaction. Finally, the ionic liquid electrolyte is left to stand at room temperature for 24 hours in the glove box filled with argon gas and moisture content less than 0.1 ppm before use. The moisture content of the prepared electrolyte is less than 50 ppm.

Battery of assembly

The cathode materials used are three-dimensional graphite (3DGr) and flake graphite (FG). Among them, the areal loading of the three-dimensional graphite is $1 \text{ mg} \cdot \text{cm}^{-2}$, with an area of $1 \times 1 \text{ cm}$. The three-dimensional graphite is purchased from Suzhou Graphene Technology Co., Ltd. As a self-supporting electrode, it can be used directly. The flake graphite electrode is prepared by mixing flake graphite (FG), conductive carbon black (Super P), and polytetrafluoroethylene (PTFE). Among them, flake graphite is purchased from Qingdao Jintao Graphite Co., Ltd., and conductive carbon black (Super P) and polytetrafluoroethylene (PTFE) are purchased from Shenzhen Kejing Co., Ltd. The mass ratio of FG: Super P: PTFE in the flake graphite electrode is 85:5:10, and then the three are mixed with water as the solvent. The mixed slurry is rolled into a self-supporting electrode with a rolling pin and vacuum-dried at 120 °C. The areal loading of flake graphite electrode is $20 \text{ mg} \cdot \text{cm}^{-2}$, with an area of $5 \times 10 \text{ cm}$. The anode material is aluminum foil with different preferred orientations. Among them, the (200) Al and (220) Al electrodes are from East Sunshine Aluminum Industry Co., Ltd. (99.99% purity, thickness is 120 μm). The (111) Al and (311) Al electrodes are made in the laboratory, and the specific preparation process is shown above. The electrolyte is $\text{AlCl}_3/\text{Et}_3\text{NHCl}$ (molar ratio of 1.5:1), and the specific preparation method is shown above. The separator is glass fiber filter paper purchased from Whatman Co., Ltd. in the UK, with a thickness of 675 microns and a pore size of 2.7 μm . The current collector is molybdenum foil, purchased from Baoji Zhongchang Nonferrous Metals Co., Ltd., with a of 99.999% and a thickness of 25 μm . The battery is assembled in a glove box where the oxygen and water content are kept below 0.1 ppm to avoid any impact on battery performance from impurities. Next, the materials are placed into the battery case in the order of cathode current collector/cathode material/separator/anode material. Then, an ionic liquid electrolyte is injected into the battery case using a pipette to ensure that the electrode sheets and separator are fully wetted with the electrolyte. Attention should be paid to controlling the injection volume to avoid overflow or insufficient electrolyte. Finally, the battery is sealed. For a Swagelok battery, it can be sealed by screwing the battery case according to the thread. For a pouch cell, a vacuum sealing machine is used for vacuum heat sealing.

Characterization

The crystalline structure of Alis was tested by X-ray diffraction (XRD, Bruker D8 Advantec diffractometer) using $\text{Cu K}\alpha$ -radiation with a scan speed of $5^\circ/\text{min}$. SEM images were measured by Field emission Scanning electron microscope (Gemini SEM 500). Electrochemical measurements of cyclic voltammetry (Scan rate is $5 \text{ mV} \cdot \text{s}^{-1}$), electrochemical impedance spectroscopy (EIS, the frequency range and amplitude of EIS test is 1,000,000–0.01 Hz and 10 mV, respectively.), and galvanostatic charge-discharge curve were conducted in the range of 0.5–2.5 V with the electrochemical workstation (Princeton) and Land CT2001 test system.

DFT calculation

The specific process of DFT calculation is completed through the ORCA5.0.3 package. Geometric optimization and absorption energy were performed using the CPCM solvent model at the B97-3c level. The dielectric constant of the ionic liquid is set to 13.5.

Data availability

All data analyzed and generated during this study are included in the article and its Supplementary Information. The data that support the plots within this paper and other findings of this study are available from the corresponding author upon request.

References

- Dunn, B., Kamath, H. & Tarascon, J.-M. Electrical energy storage for the grid: a battery of choices. *Science* **334**, 928–935 (2011).
- Thackeray, M. M., Wolverton, C. & Isaacs, E. D. Electrical energy storage for transportation—approaching the limits of, and going beyond, lithium-ion batteries. *Energ. Environ. Sci.* **5**, 7854–7863 (2012).
- Skyllas-Kazacos, M., Chakrabarti, M. H., Hajimolana, S. A., Mjalli, F. S. & Saleem, M. Progress in flow battery research and development. *J. Electrochem. Soc.* **158**, R55–R57 (2011).
- Beuse, M., Steffen, B. & Schmidt, T. S. Projecting the competition between energy-storage technologies in the electricity sector. *Joule* **4**, 2162–2184 (2020).
- Liu, Y., Zhang, R., Wang, J. & Wang, Y. Current and future lithium-ion battery manufacturing. *iScience* **24**, 102332 (2021).
- Xie, F., Zhang, L., Ye, C., Jaroniec, M. & Qiao, S. Z. The application of hollow structured anodes for sodium-ion batteries: from simple to complex systems. *Adv. Mater.* **31**, 1800492 (2019).
- Yang, J., Li, J., Gong, W. & Geng, F. Genuine divalent magnesium-ion storage and fast diffusion kinetics in metal oxides at room temperature. *Proc. Natl Acad. Sci. USA* **118**, 2111549118 (2021).
- Lin, M.-C. et al. An ultrafast rechargeable aluminium-ion battery. *Nature* **520**, 324–328 (2015).
- Massee, T. et al. Rechargeable potassium-ion batteries with honeycomb-layered tellurates as high voltage cathodes and fast potassium-ion conductors. *Nat. Commun.* **9**, 3823 (2018).
- Zhang, X. et al. Towards a stable layered vanadium oxide cathode for high-capacity calcium batteries. *Small* **18**, 2107174 (2022).
- Zhang, Q., Li, C., Li, Q., Pan, Z. & Wei, L. Flexible and high-voltage coaxial-fiber aqueous rechargeable zinc-ion battery. *Nano Lett.* **19**, 4035 (2019).
- Liu, Y. et al. Carbon nanoscrolls for aluminum battery. *Acs Nano* **18**, 2107174 (2018).
- Meng, P. et al. A low-cost and air-stable rechargeable aluminum-ion battery. *Adv. Mater.* **34**, e2106511 (2022).
- Wu, F., Zhu, N., Bai, Y., Gao, Y. & Wu, C. An interface-reconstruction effect for rechargeable aluminum battery in ionic liquid electrolyte to enhance cycling performances. *Green. Energy Environ.* **3**, 71–77 (2018).
- Xu, H. et al. Low-cost $\text{AlCl}_3/\text{Et}_3\text{NHCl}$ electrolyte for high-performance aluminum-ion battery. *Energy Storage Mater.* **17**, 38–45 (2019).
- Zhang, D. et al. Lithium hexamethyldisilazide as electrolyte additive for efficient cycling of high-voltage non-aqueous lithium metal batteries. *Nat. Commun.* **13**, 6966 (2022).
- Wang, S. et al. Space limited growth strategy for ultra-high areal capacity rechargeable aluminum batteries. *Energy Storage Mater.* **60**, 102826 (2023).
- She, D. M. et al. Erratum: surface evolution of aluminum electrodes in non-aqueous aluminum batteries. *J. Electrochem. Soc.* **167**, 149002 (2020).
- Kong, L., Xing, Y. & Pecht, M. G. Observations of lithium dendrite growth. *IEEE Access* **6**, 8387–8393 (2018).

20. Rodriguez, R. et al. In situ optical imaging of sodium electro-deposition: effects of fluoroethylene carbonate. *ACS Energy Lett.* **2**, 2051–2057 (2017).
21. Zheng, J., Yin, J., Zhang, D., Li, G. & Archer, L. A. Spontaneous and field-induced crystallographic reorientation of metal electro-deposits at battery anodes. *Sci. Adv.* **6**, eabb1122 (2020).
22. Cai, H., Bi, S., Wang, R., Liu, L. & Niu, Z. A lattice-matching strategy for highly reversible copper-metal anodes in aqueous batteries. *Angew. Chem. Int. Ed.* **61**, e202205472 (2022).
23. Zhao, Q., Zheng, J., Deng, Y. & Archer, L. Regulating the growth of aluminum electrodeposits: towards anode-free Al batteries. *J. Mater. Chem.* **8**, 23231–23238 (2020).
24. Wang, M. et al. Crystal facet correlated Zn growth on Cu for aqueous Zn metal batteries. *Energy Storage Mater.* **56**, 424–431 (2023).
25. Pradhan, D. & Reddy, R. G. Mechanistic study of Al electrodeposition from EMIC–AlCl₃ and BMIC–AlCl₃ electrolytes at low temperature. *Mater. Chem. Phys.* **143**, 564–569 (2014).
26. Lu, P. et al. Realizing long-cycling all-solid-state Li–In||TiS₂ batteries using Li_{6+x}M_xAs_{1-x}S₅I (M=Si, Sn) sulfide solid electrolytes. *Nat. Commun.* **14**, 4077 (2023).
27. Yang, Y., Liu, C., Lv, Z., Yang, H. & Li, C. Synergistic manipulation of Zn²⁺ ion flux and desolvation effect enabled by anodic growth of a 3D ZnF₂ matrix for long-lifespan and dendrite-free Zn metal anodes. *Adv. Mater.* **33**, 2007388 (2021).
28. Qin, H. et al. Building metal-molecule interface towards stable and reversible Zn metal anodes for aqueous rechargeable zinc batteries. *Adv. Funct. Mater.* **32**, 2206695 (2022).
29. Wang, Z. et al. Dendrite-free and air-stable lithium metal batteries enabled by electroless plating with aluminum fluoride. *J. Mater. Chem. A* **8**, 92189227 (2020).
30. Kwak, J. H. et al. Operando visualization of morphological evolution in Mg metal anode: insight into dendrite suppression for stable Mg metal batteries. *ACS Energy Lett.* **7**, 162–170 (2021).
31. Pei, A., Zheng, G., Shi, F., Li, Y. & Cui, Y. Nanoscale nucleation and growth of electrodeposited lithium metal. *Nano Lett.* **17**, 1132–1139 (2017).
32. Mohammadi, A., Monconduit, L., Stievano, L. & Younesi, R. Measuring the nucleation overpotential in lithium metal batteries: never forget the counter electrode. *J. Electrochem. Soc.* **169**, 070509 (2022).
33. Song, Z. et al. Uniform magnesium electrodeposition via synergistic coupling of current homogenization, geometric confinement, and chemisorption effect. *Adv. Mater.* **33**, e2100224 (2021).
34. Zhou, M. et al. Surface-preferred crystal plane for a stable and reversible zinc anode. *Adv. Mater.* **33**, e2100187 (2021).
35. Meng, Y. et al. Anode-free aluminum electrode with ultralong cycle life and high coulombic efficiency exceeding 99.92% enabled by a lattice-matching layer. *Adv. Energy Mater.* **13**, 2301322 (2023).
36. Dong, X. et al. Commercial expanded graphite as high-performance cathode for low-cost aluminum-ion battery. *Carbon* **148**, 134–140 (2019).
37. Wang, Z. Y. et al. Nickel–platinum alloy nanocrystallites with high-index facets as highly effective core catalyst for lithium–sulfur batteries. *Adv. Funct. Mater.* **32**, 2200893 (2022).
38. Xu, H. Y. et al. Low-cost AlCl₃/Et₃NHCl electrolyte for high-performance aluminum-ion battery. *Energy Storage Mater.* **17**, 38–45 (2019).

Acknowledgements

The authors gratefully acknowledge the financial support from the National Natural Science Foundation of China (Granted No. 51777152 and No. 52202296); the Natural Science Foundation of Shaanxi Province (Granted No. 2019JLZ-09, 2021JZ-01, 2021JQ-019, and 2022JQ-048); the China Postdoctoral Science Foundation (Granted No. 2020M683465). We thank Zijun Ren and Chao Li from the Instrument Analysis Center of Xi'an Jiaotong University for providing SEM and TEM measurements.

Author contributions

S.W.: Writing—conceptualization, data curation, investigation, methodology, visualization, and writing—original draft. Y.G.: Data curation, investigation, methodology, visualization, and writing—review and editing. X.D.: Conceptualization, funding acquisition, and writing—review and editing. L.X., Z.L., M.M.: Funding acquisition and writing—review and editing. Y.X., W.Y., Y.M., Y.L., and M.L.: Writing—review and editing.

Competing interests

The authors declare no competing interests.

Additional information

Supplementary information The online version contains supplementary material available at <https://doi.org/10.1038/s41467-024-50723-0>.

Correspondence and requests for materials should be addressed to Xianfeng Du.

Peer review information *Nature Communications* thanks Quanquan Pang and the other, anonymous, reviewer(s) for their contribution to the peer review of this work. A peer review file is available.

Reprints and permissions information is available at <http://www.nature.com/reprints>

Publisher's note Springer Nature remains neutral with regard to jurisdictional claims in published maps and institutional affiliations.

Open Access This article is licensed under a Creative Commons Attribution-NonCommercial-NoDerivatives 4.0 International License, which permits any non-commercial use, sharing, distribution and reproduction in any medium or format, as long as you give appropriate credit to the original author(s) and the source, provide a link to the Creative Commons licence, and indicate if you modified the licensed material. You do not have permission under this licence to share adapted material derived from this article or parts of it. The images or other third party material in this article are included in the article's Creative Commons licence, unless indicated otherwise in a credit line to the material. If material is not included in the article's Creative Commons licence and your intended use is not permitted by statutory regulation or exceeds the permitted use, you will need to obtain permission directly from the copyright holder. To view a copy of this licence, visit <http://creativecommons.org/licenses/by-nc-nd/4.0/>.

© The Author(s) 2024